

# Nonlinear Bending Mechanics of Hygroscopic Liquid Crystal Polymer Networks

**M. R. Hays**

Florida Center for Advanced  
Aero-Propulsion–FCAAP  
Department of Mechanical Engineering  
Florida A&M/Florida State University  
Tallahassee, FL 32310-6046  
Email: mrh04@fsu.edu

**H. Wang**

Florida Center for Advanced  
Aero-Propulsion–FCAAP  
Department of Mechanical Engineering  
Florida A&M/Florida State University  
Tallahassee, FL 32310-6046  
Email: hongbo@eng.fsu.edu

**W. S. Oates\***

Florida Center for Advanced Aero-Propulsion-FCAAP  
Department of Mechanical Engineering  
Florida A&M/Florida State University  
Tallahassee, FL 32310-6046

*A chemically responsive liquid crystal polymer network is experimentally characterized and compared to a nonlinear constitutive model and integrated into a finite element shell model. The constitutive model and large deformation shell model are used to understand water vapor induced bending. This class of materials is hygroscopic and can exhibit large bending as water vapor is absorbed into one side of the liquid crystal network (LCN) film. This gives rise to deflection away from the water vapor source which provides unique sensing and actuation characteristics for chemical and biomedical applications. The constitutive behavior is modeled by coupling chemical absorption with nonlinear continuum mechanics to predict how water vapor absorption affects bending deformation. In order to correlate the model with experiments, a micro-Newton measuring device was designed and tested to quantify bending forces generated by the LCN. Forces that range between 1-8  $\mu\text{N}$  were measured as a function of the distance between the water vapor source and the LCN. The experiments and model comparisons provide important insight into linear and nonlinear chemically induced bending for a number of applications such as microfluidic chemical and biological sensors.*

## 1 INTRODUCTION

Glassy and soft elastomer liquid crystal networks (LCNs) provide a number of fascinating material characteristics for solid state sensing and actuation. The synthesis of these materials was pioneered by Finkelmann and others [1–3]; however, the fundamental principles governing the

nonlinear, field-coupled mechanics are still not well understood. These active materials are of great interest for integration into micro-electro-mechanical systems (MEMS) due to their intrinsic field-coupled material behavior for use in biomedical sensing, microfluidics, and small scale robotic manipulators [4]. In such areas, polymers have received recognition due to their inherent advantages over conventional silicon materials used in MEMS. They are especially relevant in actuator and sensing environments due to their structure and color response to external stimuli, ease of implementation, and bio-compatibility.

Nematic phase liquid crystals are characterized by rigid rod shape molecules with length scales on the order of  $10 \text{ \AA}$ . When these materials are synthesized within a polymer network, monodomain or polydomain liquid crystal structures form within the polymer network. Monodomain liquid crystal structures depend on a number of processing factors such as rubbed glass slides that are used to form thin liquid crystal network films via capillary action as the material flows between the glass slides. The nematic ordering and mechanical characteristics also strongly depend on the liquid crystal density, polymer cross linking density, and temperature at cross linking [5]. The liquid crystals provide new functionality within the polymer network which can be considered as a molecular motor that does work on the polymer network. Much of the work in this area is focused on identifying methodologies to directly stimulate the liquid crystals such that an efficient transfer of energy occurs between the liquid crystals and the polymer network to create novel actuators and sensors. Various stimuli have been considered including heat, light, electrostatic fields, and chemicals [3].

---

\*Corresponding author.

The liquid crystal network considered here is a hygroscopic polymer first developed by Harris et al. [6]. The LCN initially consists of both covalent and secondary bonds. Humidity-controlled deformation occurs after the network is converted to a salt. This provides a hygroscopic material which begins to swell under humid conditions as water infiltrates the material and interacts with the liquid crystals that are attached to the polymer network. Different deformation may also occur if the pH or polarity of the solvent in the environment changes [7]. The LCN material deforms due to asymmetric water vapor absorption which can occur on the order of seconds. The liquid crystal salt units are believed to expand perpendicular to the director that is pre-aligned in the liquid crystalline phase. It will be shown that this preferred expansion depends on the transverse isotropic elastic properties of the film which depend on the alignment of the liquid crystals. Order-disorder liquid crystal evolution can also play a role in the deformation process which is also briefly discussed. It will be shown that if only one side of the LCN is exposed to moisture, asymmetric swelling causes the polymer to bend away from the water source as illustrated in Figure 1.

In the following sections, the bending force measurements of the LCN film is presented and compared with a nonlinear continuum model. The constitutive model includes nonlinear mechanics, diffusion of water vapor, and a chemical potential associated with interactions between the salt units and water vapor absorption. The constitutive model is incorporated into an orthotropic nonlinear shell finite element model and correlated with the experimental results. Discussion and concluding remarks are given in the final section.

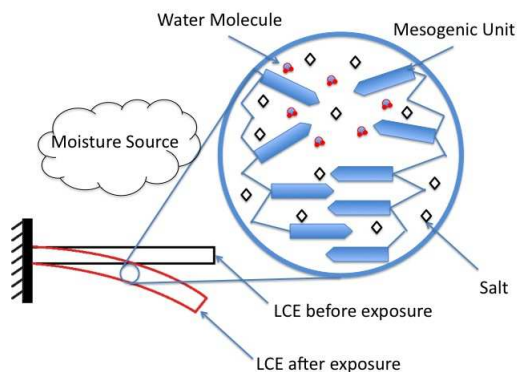


Fig. 1. Illustration of the bending mechanism caused by asymmetric swelling of the hygroscopic liquid crystal network.

## 2 EXPERIMENTAL SETUP

The synthesis of the hygroscopic liquid crystal network is based on the materials and a synthesis procedure described elsewhere [6]. Capillary forces were used to form a monodomain film between rubbed glass slides. The final poly-

mer network film thickness was controlled using spacers between the glass slides which resulted in a film thickness of  $26 \mu\text{m}$ . All specimens were stored in a desiccant container until tested. The specimen length and width used in all experiments were  $8.8 \times 2.6 \text{ mm}^2$  unless otherwise noted.

Prior to conducting bending force measurements, the film was placed over water and the direction of maximum bending was identified experimentally. The specimens were cut in a direction such that the long axis of the cantilever film exhibited the largest amount of bending. Based on the water vapor bending characterization presented in [6], the long axis of the film is designated to be perpendicular to the director. The bending forces were tested using the following set-up and procedure for this material and structure configuration.

### 2.1 BENDING MODE MEASUREMENTS

A custom designed mechanical measuring device was developed to measure micro-Newton bending forces generated by the liquid crystal network. A small diameter stainless steel wire (McMaster-Carr P/N: 9882K11, measured diameter:  $120 \mu\text{m}$ ) was placed in contact with the polymer network and viewed under an optical microscope. The deflection of the wire was measured using an Olympus BX60 microscope with a QImaging Go-3 camera to quantify the force generated based on elastic properties and bending mechanics of the wire.

In order to ensure sufficient precision of the measurements, the elastic modulus of the stainless steel wire was measured using both tensile test and harmonic resonance tests. The wire was tensile loaded on a MTS 1 kN testing machine equipped with a 5 N load cell. An average elastic modulus of 24.28 GPa with a standard deviation of 0.82 GPa was measured using five different specimens. The mechanical behavior was found to be linear elastic up to at least  $3000 \mu\epsilon$ . This modulus measurement was compared to resonance tests. In these test, the wire was clamped on one side and the free side was placed under a microscope to optically measure small magnitudes of free vibration. Once the wire was deflected and released, a high speed camera (10,000 fps) was used to measure the damped resonance frequency of the wire. Using vibration dynamics and taking into account damping, the elastic modulus was calculated from the damped natural frequency of the wire. The elastic modulus of the stainless steel wire was found to be 24.30 GPa with a standard deviation of 0.29 GPa for 6 different measurements on the same wire. The wire used in the resonance test was used in all force measurements. Given the elastic modulus and geometry of the wire, the force required for a given displacement was determined using classic bending mechanics by assuming a uniform circular cross-section geometry. Given the maximum force measured in the experiments ( $\sim 8 \mu\text{N}$ ), the force measurement uncertainty was approximately  $\pm 93 \text{ nN}$  based on the dynamic measurement standard deviation.

The magnitude of force generated by the liquid crystal network in the presence of water vapor was measured by placing the actuator in line with the calibrated stainless steel

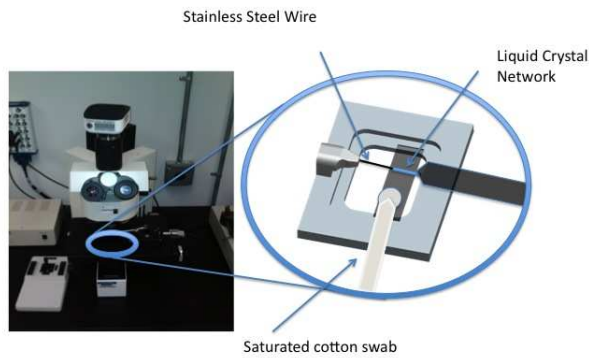


Fig. 2. The experimental set-up that illustrates the technique used to indirectly measure forces using the stainless steel wire using an optical microscopy set-up.

wire as shown in Figure 2. The film was fully constrained on one end and in contact with the stainless steel wire on the other end. A fully saturated moisture sheet consisting of a cotton swab on the end of a rod was attached to a translating stage to control the amount of water vapor exposure as shown in Figure 2. When the stage was moved, the saturated cotton swab moved in the direction of the liquid crystal network. The film would then bend in a direction away from the water vapor source as the distance between the water vapor source and film was reduced. The deflection of the wire was measured optically under the microscope. The distance between the water vapor source and the film was quantified using calibrated measurement software with the digital camera that was mounted on the microscope. This distance was taken from a reference position of the film prior to bending. The bending forces are plotted in Figure 3 which show increases in forces from  $1 \mu\text{N}$  to  $8 \mu\text{N}$  as the water vapor source approaches the film. It is noted that this is not the blocking force, but the force induced against a “spring-like” load created by the wire in contact with the film. It will be shown through model comparisons that this force is within 1% of the blocked force.

## 2.2 LCN Modulus Characterization

The elastic modulus of the LCN was also measured and compared with data in the literature. Due to the delicate nature of the films, the modulus was measured using the stainless steel wire and optical microscopy set-up. The stainless steel wire was placed on a translating stage that moved perpendicular to the longitudinal axis of the specimen. The film was again constrained on one end and was placed in contact with the steel wire on the opposing end as shown in Figure 2. The base of the steel wire was displaced a prescribed amount and magnitudes of deflection of both the liquid crystal network and the wire were recorded while in contact. Using

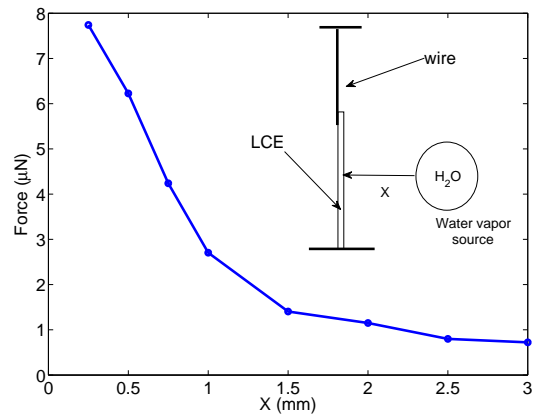


Fig. 3. Experimental results of bending forces generated by the LCN film that is measured with the stainless steel wire.

classical bending, the elastic modulus of the LCN was determined [8]. The elastic modulus of the cantilever was found to be  $122.46 \text{ MPa}$  with a standard deviation of  $5.71 \text{ MPa}$  for five different specimens. Results presented in [9] have shown that the elastic modulus is orthotropic where the modulus perpendicular to the liquid crystal director was  $1.6 \text{ GPa}$  and  $2.4 \text{ GPa}$  parallel to the director. These values were obtained in a dry state. In a water swollen state, the moduli were  $0.16 \text{ GPa}$  and  $0.3 \text{ GPa}$  perpendicular and parallel to the director, respectively.

Since the modulus measured in bending was significantly lower than dynamic mechanical analysis (DMA) data reported in the literature [9], the assumption of classic beam bending was assessed by determining the modulus as a function of the point of wire contact along the long axis of the LCN film. A similar analysis is reported in [10] which showed significant reductions in modulus measurements in polymer microcantilevers in comparison to bulk tensile tests. The stainless steel wire was placed in contact with the LCN film at different points along the long axis and the stiffness was computed again based on classic beam theory. The modulus was found to be approximately constant based on these measurements as shown in Figure 4; however, the nominal modulus was only  $6 \text{ MPa}$ . It is important to note that these modulus measurements were conducted on a different specimen that was synthesized several months after the original experiments were conducted. A reduction of the modulus on the order of one magnitude was measured relative to the original measurements conducted during the time of the water absorption force measurements. Due to the reduction in modulus, images were taken under a load for the smallest and largest normalized distances and were compared with classic beam displacement solutions. The results illustrated good comparisons with beam theory for both extreme cases; see the Appendix for comparisons of data and classic beam displacement solutions. Based on the uncertainty in modulus,

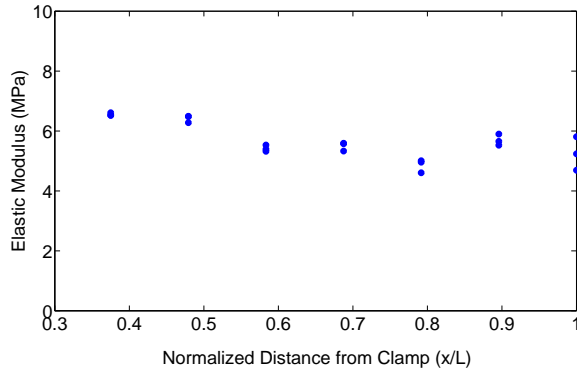


Fig. 4. Variations in the elastic modulus based on classic beam theory of a cantilever under a point load. Multiple measurements were taken at each normalized distance  $x/L$ .

the DMA modulus measurement given in [9] was used in the finite element shell model. The effect of changes in elastic modulus on changes in concentration and bending deformation will also be assessed using the model.

It was previously noted in these experiments that the films were cut in the direction which produced the largest bending along the long axis of the cantilever specimens. This is assumed to be the direction perpendicular to the director which would coincide with the measurement of a lower elastic modulus relative to the modulus parallel to the director. In the following model comparison, it is assumed that the elastic modulus parallel to the director (perpendicular to the cantilever film's long axis) is 1.5 times as large as the measured modulus.

### 3 Nonlinear Mechanics Modeling

The bending behavior of the liquid crystal network is modeled by coupling diffusion of water vapor with nonlinear continuum mechanics. To this end, an energy function is introduced that includes a chemical potential energy function and a mechanical energy function of the host polymer network. This is coupled with mass diffusion to describe the rate of water vapor absorption into the material. The chemical potential energy function is used to describe the chemical affinity for water molecules to absorb into the film via interaction with the salt units. The concentration of the water molecules is introduced as an internal state variable to describe this interaction. Since changes in bending were measured as a function of position of the water vapor source, diffusion of water vapor in the air surrounding the film is also modeled using diffusion relations described in [11]. The differences in water vapor diffusion in air and within the liquid crystal network are described in the following subsections.

It has been previously reported that the salt units within the liquid crystal network prefer to expand perpendicular to the director during water absorption. This is believed to be due to the transverse isotropic elastic properties which are

characterized by larger stiffness parallel to the director. Using nonlinear mechanics, it is shown that a scalar order parameter induces hydrostatic stresses. This is expected since a scalar order parameter has no preferred orientation. Since the polymer network is transverse isotropic due to the monodomain liquid crystal order, the strain induced by the hydrostatic stress will lead to more bending along the compliant direction (i.e., perpendicular to the director) which is similar to experimental observations.

It is important to note that during water absorption, order-disorder liquid crystal evolution could directly lead to anisotropic deformation. The proposed model focuses on the lowest-order scalar order parameter contribution to deformation in terms of concentration. Vector order parameter effects could be introduced into the model to explicitly include the liquid crystal director ( $n_i$ ) using Landau-de Gennes free energy relations. This typically requires introducing an eight order polynomial in  $n_i$  or fourth order polynomial in  $Q_{ij} = Q/2(3n_i n_j - \delta_{ij})$ ; see [3, 12] for details. These higher order effects require careful treatment of the director order reduction to ensure  $Q_{ij}$  remains traceless during order-disorder processes. This will be described in a future analysis [13].

### 3.1 Chemical Potential Coupled Nonlinear Mechanics

The chemical free energy is written as a function of the water vapor concentration

$$\Psi_c(c_w) = \frac{g}{2}(c_w - c_0)^2 + \frac{h}{4}(c_w - c_0)^4 \quad (1)$$

per current volume where  $c_w$  is the concentration of water in moles per volume in the liquid crystal network and  $c_0$  is a reference concentration at room temperature, pressure, and relative humidity. Whereas the number of moles is often used in formulating a chemical potential [14, 15], the concentration is used as the internal state variable to obtain stress as a function of water vapor. The amount of water concentration will be quantified using relative humidity and ideal gas relations in Section 3.3. The phenomenological parameters  $g$  and  $h$  denote the magnitude of the linear and third order chemical potential driving forces, respectively.

The chemical potential in the spatial configuration is defined to be work conjugate to the concentration of water vapor

$$\mu = \frac{\partial \Psi_c}{\partial c_w} \quad (2)$$

which follows the classic description [15]. More details on the differences of these field variables in the spatial and reference configuration is described in [16] and in Section 3.2. It will be shown that a linear chemical potential is sufficient to predict small bending deformation while third order effects are important in predicting larger bending deformation.

Nonlinear coupling between the deformation gradient and the water concentration is introduced within this energy function using the conservation of mass relation between the reference and spatial configurations,  $c_w = J^{-1}\tilde{c}_w$ , where  $J = \det(F_{iK})$  is the Jacobian and  $F_{iK}$  is the deformation gradient [17]. The concentration in the reference configuration is denoted by  $\tilde{c}_w$ . This requires that the free energy in the reference frame be coupled to the deformation gradient according to

$$\tilde{\Psi}_c = \frac{gJ}{2}(J^{-1}\tilde{c}_w - c_0)^2 + \frac{hJ}{4}(J^{-1}\tilde{c}_w - c_0)^4 \quad (3)$$

per reference volume, noting that  $\tilde{\Psi}_c = J\Psi_c$  [18].

The stress associated with the change in water vapor concentration is obtained from the conventional definition of nominal stress,  $s_{iK} = \frac{\partial\tilde{\Psi}}{\partial F_{iK}}$  where  $\tilde{\Psi}$  is the total free energy of the solid material [18]. In this case, the water vapor coupled stress is defined by  $s_{iK}^c = \frac{\partial\tilde{\Psi}_c}{\partial F_{iK}}$ . The functional form of this stress tensor is

$$s_{iK}^c = -\frac{g}{2}J^{-1}H_{iK}(\tilde{c}_w^2 - J^2c_0^2) - \frac{h}{4}H_{iK}(3J^{-3}\tilde{c}_w^4 - 8J^{-2}\tilde{c}_w^3c_0 + 6J^{-1}\tilde{c}_w^2c_0^2 - Jc_0^4). \quad (4)$$

The Cauchy stress is often useful in giving concise constitutive relations and in illustrating stress symmetry. This stress can be obtained from the nominal stress using

$$\sigma_{ij}^c = J^{-1}F_{jK}\frac{\partial\tilde{\Psi}_c}{\partial F_{iK}} \quad (5)$$

as described in [17] for the general case. This gives

$$\sigma_{ij}^c = -\left(\frac{g}{2}(c_w^2 - c_0^2) + \frac{h}{4}(3c_w^4 - 8c_w^3c_0 + 6c_w^2c_0^2 - c_0^4)\right)\delta_{ij} \quad (6)$$

for the concentration coupled Cauchy stress which illustrates that changes in water concentration lead to hydrostatic stresses. In the experiments, the amount of bending in the film was limited to the small strain case; therefore, the concentration coupled Cauchy stress will be introduced into the bending moment calculations for nonlinear shell modeling. While the strain is small, large rotation may be observed in certain cases which motivates the need for using nonlinear plates or shells. This is discussed in Section 3.4.

### 3.2 Elastic Coupling and Diffusion Behavior

The chemical potential energy given by (3) is combined with elastic energy to describe the mechanical behavior of

the host polymer network. A linear elastic energy function is introduced to model the mechanical behavior; however, the theory can accommodate any mechanical energy such as hyperelastic neo-Hookean, Ogden, Mooney-Rivlin, etc.; see [19] for an example on soft liquid crystal elastomers using a neo-Hookean model. The elastic energy used here is

$$\tilde{\Psi}_M = \frac{c_{IJKL}}{2}E_{IJ}E_{KL} \quad (7)$$

where  $c_{IJKL}$  is the fourth order elastic tensor in the reference description and  $E_{IJ}$  is the Green strain tensor [17]. This will be reduced to transverse isotropic elastic properties when implemented in the finite element shell model such that a larger stiffness is implemented in the orientation of the director. This gives a reasonable estimate of these liquid crystal networks in the glassy state prior to significant water absorption. As water penetrates the material, reductions in modulus may lead to incompressible elastomer behavior. The uncertainty in gradients of modulus and changes in the Poisson ratio towards an incompressible state (i.e.,  $\nu \Rightarrow 0.5$ ) will be assessed using the model.

The total free energy is defined by the sum of the chemical potential and mechanical free energy as denoted by  $\tilde{\Psi} = \tilde{\Psi}_c + \tilde{\Psi}_M$ . The change in this free energy with respect to deformation and concentration provides stress and chemical driving forces; respectively. When combined with kinetic energy, the variation in deformation leads to the linear momentum equations which will be implemented in terms of a finite element shell model in the following section. The chemical potential driving force is introduced into the conservation of mass which results in a diffusion equation. This is used to model water vapor concentration gradients that occur through the thickness of the LCN film. The concentration gradient is introduced into the coupled Cauchy stress given by (6) to calculate the induced bending moment from water vapor absorption. This moment will be applied to the nonlinear shell model to simulate bending from water vapor concentration gradients. In addition, diffusion of water vapor through air will be analyzed to quantify changes in bending forces as the water vapor source moves closer to the liquid crystal network.

The evolution of water vapor concentration is governed by

$$\tilde{c}_w = -\tilde{J}_{I,I} \quad \text{in } \Omega_0 \quad (8)$$

where  $\Omega_0$  is the reference volume and  $\tilde{J}_I$  is the mass flux in the reference configuration. This flux can be related to the flux in the spatial configuration using the transformation,  $J_i = J^{-1}F_{iK}\tilde{J}_K$  [16]. It is also important to point out that the diffusion in the spatial frame is proportional to the relative velocity between the solid and the diffusing chemical [11, 16]. The mass flux is assumed to be proportional to the gradient of the chemical potential

$$\tilde{J}_I = -A_{IJ}\tilde{\mu}_{,J} \quad (9)$$

where the chemical potential in the reference configuration is  $\tilde{\mu} = \frac{\partial \tilde{\Psi}}{\partial \tilde{c}_w}$ . The mobility tensor is denoted by  $A_{IJ}$  [20].

A diffusion equation is obtained by substituting (9) into (8). In the numerical model, the mobility tensor is assumed to be isotropic and independent of concentration  $A_{IJ} = D\delta_{IJ}$ . A correlation between water vapor in the air and inside the material is determined based on the experiments. This requires determining steady state diffusion within the LCN film to quantify bending. It also requires determining steady-state diffusion in air between the water source and the film surface. Since steady-state diffusion is of primary interest for experimental comparisons, the value of  $D$  is arbitrary in the model.

Using the above diffusion relations, the final form of the time-dependent conservation of mass in the reference configuration is

$$\tilde{c}_w = D\tilde{\mu}_{,II}. \quad (10)$$

This relation is used to predict: i) the change in water concentration on the surface of the film with respect to the location of the water vapor source in the air and ii) the diffusion of water into the LCN film through the material thickness. In regards to (i), this is necessary to relate changes in bending as the water source approaches the film surface based on bending force changes illustrated in Figure 3. This will also be important in modeling the case of large film rotation since the concentration may vary along the length of the LCN film.

The diffusion equation in (10) is first used to correlate steady state concentration of water vapor in air from a reference distance between the water source and the LCN film surface. These values are then used to correlate the amount of water present on the film's surface and the penetration into the material thickness as a function of the distance from the water vapor source. Steady state values are used to compare with static deformation measurements given in the previous section.

### 3.3 Water Vapor Concentration

As outlined in [11], the flux in air is attributed to a combination of diffusion and flux from the total molar bulk flow. A one dimensional solution is used since the water vapor source was a flat, damp cotton swab that was larger than the film. In this case, a close form solution for the water vapor concentration is given by

$$\left( \frac{1 - \frac{\tilde{c}_w}{c}}{1 - \frac{\tilde{c}_{max}}{c}} \right) = \left( \frac{1 - \frac{c_0}{c}}{1 - \frac{\tilde{c}_{max}}{c}} \right)^{\frac{X}{X_0}} \quad (11)$$

where  $\tilde{c}$  is the total concentration of the air and water vapor,  $\tilde{c}_{max}$  is the maximum water vapor concentration at the surface of the moisture source, and  $c_0$  is the water vapor concentration at ambient conditions. The reference distance between the film surface and the moisture source is defined by  $X$  while  $X_0$  is the distance to ambient conditions.

For the relative humidity conditions in the experiments, this relation results in a linear decay of water vapor concentration from the reference distance  $X_0$  where the humidity induced bending is zero. This reference position is restricted to  $X > 3$  mm (see Figure 3) and defined to be  $X = X_0 = 4$  mm in the model since the bending force does not go completely to zero at  $X = 3$  mm. The boundary conditions for the diffusion problem include a fixed concentration of water vapor at  $X = 0$  and the concentration of water vapor in the air is set to ambient conditions at  $X = X_0 = 4$  mm. The size of the water vapor source is large relative to the size of the LCN film such that variations along the length and width of the film are negligible for small film rotations. For large rotations, the concentration variation along the length may contribute to changes in bending. These changes will be compared to the ideal model that assumes constant concentration along the film length.

Whereas the concentration of water vapor in air at steady-state that is based on (11) is nonlinear in general, this relation simplifies to a linear decay over the experimental conditions tested. Therefore, the concentration is written as

$$\tilde{c}_w(X) = a(X_0 - X) + c_0 \quad \text{for } 0 \leq X \leq X_0 \quad (12)$$

where the parameter  $a$  is obtained from (11) and depends on the ambient and saturated air conditions at room temperature, atmospheric pressure, and relative humidity. The ambient concentration  $c_0$  is obtained at room temperature and pressure for the nominal relative humidity measured during the experiments which was measured to be 35%.

The water concentration in air is obtained using the following method. Based on the ideal gas law and a volume of gas above the LCN film, the ambient concentration for a 35% relative humidity is  $c_0 = 3.97 \times 10^{-7}$  mol/m<sup>3</sup>. The volume of gas used in this calculation is based on dimensions corresponding to the film geometry and maximum distance from the water vapor source ( $8.8 \times 2.6 \times 3$ ) mm<sup>3</sup> where the last dimension corresponds to the distance from the film surface to the water vapor source:  $X = 3$  mm. It is assumed that the volume of gas near the film surface becomes fully saturated when  $X = 0.25$  mm. Since the water concentration scales linearly with the relative humidity, the maximum concentration is  $c_{max} = 1.13 \times 10^{-6}$  mol/m<sup>3</sup> for a relative humidity of 100%; see the Appendix for details on these calculations.

Inside the LCN film, the water vapor concentration decreases through the thickness to  $c_0$  on the back side of the film. In the case where  $g \neq 0$  and  $h = 0$  in (1), the steady-state solution is trivially satisfied by a linear decay. It will be shown that including the fourth order term in (1) is necessary to fit the bending force data to experimental results for

larger bending forces. This results in a nonlinear diffusion equation that is solved numerically using the pdepe solver in Matlab. The steady-state solution is then fit to a polynomial equation and used to obtain stresses and moments within the liquid crystal network. The polynomial fits are denoted by

$$\tilde{c}_w = f(X, Z) + c_0 \quad (13)$$

where the function  $f(X, Z)$  is linear if  $g \neq 0, h = 0$  and nonlinear if  $g = 0, h \neq 0$  as illustrated in Figures 5 and 6; respectively. In these simulations, the time dependent water vapor concentration has been normalized as well as the material coordinate through the film thickness. The polynomial fits are taken at steady state. The coordinate  $Z$  is within the LCN film thickness and  $X$  corresponds to the distance between the water vapor source and the film surface in the reference configuration. These coordinates are parallel and therefore directly related; however, they are distinguished here to emphasize the change in location of the water vapor source. Furthermore, the range of  $X$  is on the order of millimeters while the range of  $Z$  is on the order of  $10 \mu\text{m}$ ; therefore, the coordinate  $X$  is practically constant through the film thickness for a fixed position of the water vapor source. The values for the polynomial fits for steady state diffusion are given in the Appendix.

The relation in (13) is substituted into the Cauchy stress relation (6) to quantify bending moments and bending strain induced by the water concentration gradients in the liquid crystal network film. The moments in the  $X$  and  $Y$  directions are obtained based on the Cauchy stresses for implementation in the finite element model. For the case of large rotation,  $\tilde{c}_w \neq c_w$  will be implemented by tracking the film surface during quasi-static bending and updating the water vapor induced bending moment along the surface of the film.

The water vapor induced stress couple is

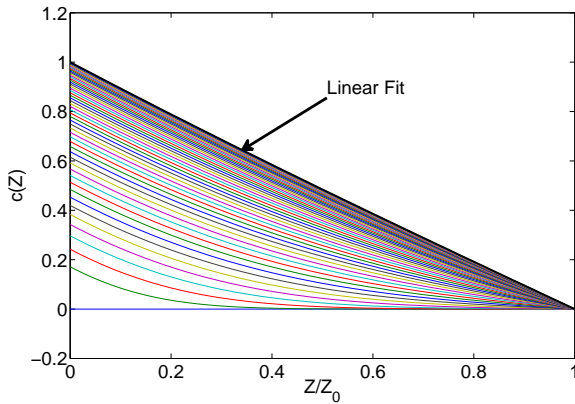


Fig. 5. Time dependent solutions of diffusion of water vapor into the liquid crystal network. Each line corresponds to a time step starting from zero initial conditions at  $t = 0$ . Results are plotted for a linear chemical potential where  $g \neq 0$  and  $h = 0$ . The linear fit is given at steady-state.

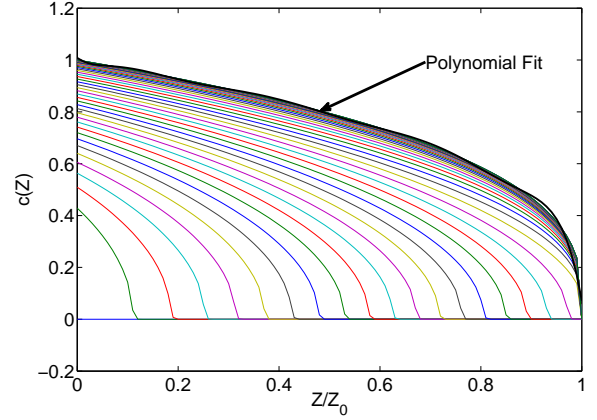


Fig. 6. Time dependent solutions of diffusion of water vapor into the liquid crystal network. Results are for a nonlinear chemical potential where  $g = 0$  and  $h \neq 0$ . Again, the polynomial fit is given at steady-state.

$$\mathbf{m}^c = \frac{1}{\bar{j}} \int_{-t/2}^{t/2} \boldsymbol{\sigma}^c \mathbf{g}^\alpha j \xi d\xi \quad (14)$$

where  $\bar{j}$  is the mid-surface Jacobian,  $\mathbf{g}^\alpha$  is the reciprocal convected basis for the shell surface,  $j$  is the determinant of the tangent map of deformation, and  $\xi$  is the coordinate through the film's thickness  $t$ ; see [21] for more details. Note that due to the hydrostatic concentration stress  $\boldsymbol{\sigma}^c$ , the shear stress couple  $m_{xy}^c$  is zero and the normal stress couples are equal,  $m_{xx}^c = m_{yy}^c$ .

The concentration dependent stress couple in (14) is correlated with internal bending strains to facilitate its integration into FEAP. As discussed in [22], the stress couple is work conjugate to the bending strain according to  $m_{ij} = \frac{\partial \psi}{\partial \kappa_{ij}}$  where  $\psi$  is the internal energy and  $\kappa_{ij}$  is the bending strain relative to the mid-surface. For the case of concentration induced bending, the strain induced by the concentration is determined from

$$\boldsymbol{\sigma}_{ij} = c_{ijkl} (\boldsymbol{\epsilon}_{kl} - \boldsymbol{\epsilon}_{kl}^c) \quad (15)$$

where  $\boldsymbol{\epsilon}_{kl}^c$  is the concentration induced strain in the deformed state. The bending strain can be obtained through correlations with the concentration induced stress in (6). This is given by

$$m_{ij}^c = - \int_{-t/2}^{t/2} c_{ijkl} \boldsymbol{\epsilon}_{kl}^c \xi d\xi = - \int_{-t/2}^{t/2} c_{ijkl} \boldsymbol{\kappa}_{kl}^c \xi^2 d\xi \quad (16)$$

where the last relation on the right is defined in terms of the bending strain induced by concentration gradients and

is equivalent to the actual strain  $\varepsilon_{kl}^c$  only in the integral sense. This is because the additional effect of uniform or membrane strain does not contribute to bending. This allows the bending strain induced by concentration to be directly introduced into FEAP. For simplicity, the small deformation case has been considered where  $\bar{j} = j \simeq 1$  and the reciprocal connected basis is aligned with the global Cartesian coordinate system for a flat film.

For orthotropic elastic materials, the bending strain induced by the concentration gradient is equivalent in both directions and given by

$$\kappa^c = \frac{12(1-\nu)m_{yy}^c}{t^3 E_x} = \frac{12(1-\nu)m_{xx}^c}{t^3 E_y} \quad (17)$$

where the moment is numerically calculated using (14), (6), and the concentration gradient through the thickness. The orthotropic moduli are denoted by  $E_x$  and  $E_y$ .

These relations are implemented in the following section using the nonlinear finite element shell model to accommodate the bending moment induced by the water vapor concentration and the internal mechanical moment induced by the elasticity of the polymer network as well as external forces from the stainless steel wire in contact with the film. Since these films may undergo large rotation, the large deformation shell model is used to correlate the measured bending forces with the internal moment induced by the changes in water vapor concentration.

### 3.4 Nonlinear Bending Mechanics

The bending force measurements due to water vapor are compared with the induced moment in (14) using the finite element analysis program FEAP [23]. The shell model contained within FEAP is based on an exact three dimensional geometrical description of thin shells that can undergo large deformation. A series of papers on the theory can be found in [21,22,24,25]. The model utilizes classical shell theory as described by a one-director Cosserat surface which leads to an efficient numerical algorithm that can handle extremely large deformation. The approach mitigates shear or membrane locking such that larger deformation problems can be simulated.

A flat plate geometry is implemented to describe the liquid crystal network film geometry. The boundary conditions include the following set of constraints. Similar to the experiments, one end of the film was fully clamped. On the opposing end, the center node along this free edge was constrained to the experimental displacement in the presence of the stainless steel wire. Recall that the bending force was measured based on deflection of a wire of known geometry and stiffness. Model correlation to this measurement was obtained by applying the concentration dependent bending strain in (17) uniformly over the entire surface of the model to predict the effect of water vapor induced bending. The displacements were small when the film was constrained by the wire; therefore, changes in concentration along the length

of the shell surface due to displacements were neglected in these simulations. In the case of free bending displacement, concentration dependence on bending displacements is evaluated. The moment was increased until the reaction force at the node constrained to a fixed displacement matched the forces from the experiments. This was done for each position of the water vapor source. Through this process, the water vapor induced moment was calculated at each experiment point as illustrated in Figure 7. These calculations utilize (14)-(17) to describe the concentration induced bending strain for each relative humidity condition.

The elastic modulus along the long axis of the film was based on data given in [6]. Since the long axis of the film was oriented in the direction of largest bending, this direction is assumed to coincide with the direction perpendicular to the liquid crystal director. Based on modulus measurements given in [7], the elastic modulus parallel to the director is nominally 1.5 times larger in the direction parallel to the director. This proportionality was applied to the model. The Poisson ratio was assumed to be 0.35 since these films are glassy in the “dry” state and unlikely to be incompressible in this state. The constant modulus assumption and Poisson ratio introduces some uncertainty into the moment predictions since it is known that the elastic behavior changes significantly between the extremes of a dry and completely water swollen state. This uncertainty is reduced by implementing an effective modulus that is a function of the water concentration. This “dry” state modulus was assumed to be the modulus in ambient humidity conditions. The modulus then varied linearly with the water concentration. An effective modulus was obtained by integrating the modulus over the film thickness and then normalizing it by the thickness. The effective modulus perpendicular to the director varied from 1.6 GPa in a dry state where  $X = 3$  mm to 360 MPa for the largest bending state where  $X = 0.25$  mm. This calculation used the nonlinear distribution of the water concentration since this distribution and coupled stresses provided a better model fit over a larger range of the experimental conditions. The uncertainty in the modulus is discussed and compared with different modeling techniques in subsequent paragraphs.

Since the calculation of the moment is based directly on experiments, it is not ideal for general model predictions for variations in concentration near the film surface. A stronger understanding of the material behavior is obtained by implementing a material parameter fit using the parameters in (1) and (13). Improved model correlation is obtained using the steady-state diffusion solution with  $h = 1.35 \times 10^{26}$  Nm<sup>9</sup>/mol<sup>4</sup> and  $g = 0$  in comparison with  $g = 9.0 \times 10^{13}$  Nm<sup>3</sup>/mol<sup>2</sup> and  $h = 0$  as shown in Figure 7. These model fits illustrate that a linear chemical potential where  $h = 0$  is sufficient to predict bending at lower concentrations, while higher order nonlinear effects ( $h \neq 0$ ) are required for higher water vapor concentrations.

The model fit was then used to predict the free bending of the LCN film. Using the effective modulus, maximum free displacement simulations are plotted in Figure 8. In this plot, a comparison of bending as a function of water vapor

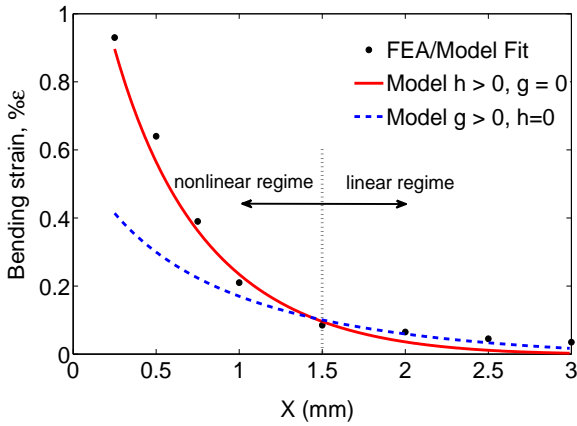


Fig. 7. Model predictions based on the moment calculated using the bending force data and the FEAP nonlinear shell model. These calculations are compared with the general stress couple model using (14) by varying the chemical potential parameters  $g$  and  $h$ . The dashed curve uses  $g = 9.0 \times 10^{13} \text{ Nm}^3/\text{mol}^2$  and  $h = 0$  and the solid curve uses  $h = 1.35 \times 10^{26} \text{ Nm}^9/\text{mol}^4$  and  $g = 0$ . The linear and nonlinear regimes refer to the form of the chemical potential driving force.

concentration variations during large bending deformation is analyzed. The shell displacement is predicted by comparing the two cases: 1) constant concentration induced bending strain that is independent of the mid-surface position of the shell and 2) concentration induced bending strain as a function of the film surface during large rotation. The concentration induced bending strain is incremented during quasi-static loading to avoid transient waves in the solution. It is shown that changes in concentration along the film length during large rotation has a significant effect on the free bending prediction. This is expected since the concentration induced bending strain is highly sensitive to positions between  $X = 0.25 \text{ mm}$  and  $X = 1.0 \text{ mm}$ ; see Figure 7 in comparison with Figure 8.

In Figure 9, free displacement predictions are plotted for two different positions of the water vapor source that were measured experimentally. Again, the case of position dependent concentration relative to the film surface (“true” solution) is plotted and compared with the case where changes in concentration as a function of large bending rotation are neglected (“ideal” solution). The results demonstrate high sensitivity to water vapor as significant bending rotations begin to occur when the water vapor source approaches the film surface. The comparison between the “true” and “ideal” solutions illustrate significant deviations in bending displacement for small values of  $X$  since the sensitivity of water vapor increases as  $X$  decreases as previously illustrated in Figure 7. Also note that under these free displacements, only minor in-plane displacement coupling was predicted. Thus, a decoupled linear plate model could be used in this operating regime. However, larger displacements have been observed

experimentally and will be illustrated through a chemical potential parameter sensitivity analysis.

The uncertainty associated with the free displacement model predictions is quantified by implementing elastic properties that vary through the thickness. Again the elastic tensor was assumed to be proportional to the water concentration by varying the modulus perpendicular to the director from 1.6 GPa in a dry state to 122 MPa in a saturated state. The modulus was increased by a factor of 1.5 parallel to the director. A two dimensional domain was implemented in Comsol 3.5 to quantify variations through the thickness. A smaller film length was simulated to resolve concentration and stress variations through the thickness. Pure bending was modeled by constraining one bottom corner as a pin and the opposing bottom corner as a roller. Based on the nonlinear absorption model where  $g = 0$  and  $h > 0$ , the curvature was compared for a thickness varying modulus versus the effective modulus model. The curvature was found to be comparable for water vapor concentrations for  $X \geq 1.5 \text{ mm}$ . When  $X \leq 1.0 \text{ mm}$ , significant errors on the order of 30% occurred. This error is expected to be an upper bound since the modulus reported in the literature compares a “dry” state to a specimen that was fully submersed in water. Smaller changes in stiffness are expected when the material is only exposed to water vapor in the air. The effect of the Poisson ratio ( $\nu$ ) was also checked. The difference in deflection in the shell model using  $\nu = 0.35$  versus  $\nu = 0.5$  was negligible.

It was previously noted that the forces measured and illustrated in Figure 3 are not the blocked forces. These measurements are predicted to be relatively close to the blocked forces. By fixing the displacement at the end of the shell model to be zero, the blocked forces were computed using the nonlinear shell model and water vapor induced moments. These forces were less than 1% different than the measured forces. This becomes apparent when considering the dis-

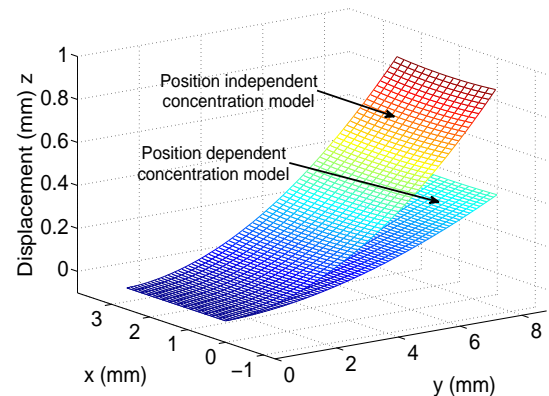


Fig. 8. Bending deformation for the maximum bending force case where  $X = 0.25 \text{ mm}$ . The results are given for the free displacement case (no external edge load) for the case where concentration is independent or dependent on the bending deformation of the film.

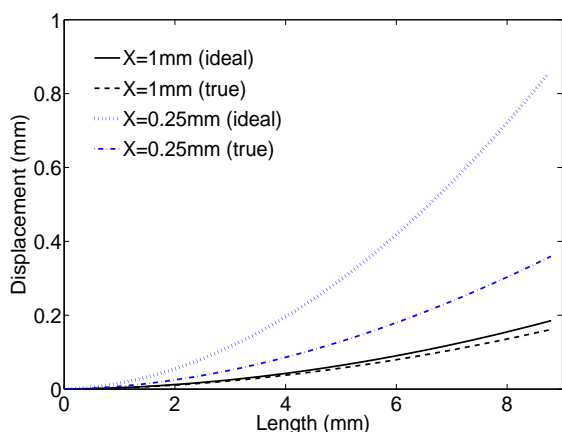


Fig. 9. The cross section view of the shell model illustrating increases in bending with no external load. The displacements correspond to two experimental water vapor locations ( $X = 1$  mm and  $X = 0.25$  mm) previously illustrated in Figure 7. The “true” solutions correspond to position dependent concentration while the “ideal” solution neglects position dependent concentration.

placements and bending forces of the film measured optically. These displacements in the presence of the stainless steel wire were on the order of 1 to 10  $\mu\text{m}$  which are about three orders of magnitude smaller than the free displacement model predictions.

Lastly note that these materials fatigue as they are continuously exposed to water vapor. Larger free bending was observed prior to conducting quantitative bending force measurements. Similar larger bending has been reported in the literature where rotation greater than  $90^\circ$  has been observed [6]. Based on these observations, the sensitivity of the chemical free energy parameter  $h$  was conducted using the nonlinear shell model. As illustrated in Figure 10, large bending is obtained by increasing the fourth order parameter  $h$  by factors ranging from 2 to 8. The angle of the film at the end was  $24^\circ$ ,  $50^\circ$ , and  $100^\circ$  for  $h$  parameters that increased by factors ranging from 2, 4, and 8; respectively. It is also important to note that these larger bending angles required assuming constant concentration over the length of the film.

#### 4 CONCLUDING REMARKS

The bending forces of a hygroscopic liquid crystal network film were measured and compared to a finite deformation constitutive model that was integrated into a nonlinear shell model. The results show micro Newton forces can be generated by a film with geometry  $8.8 \times 2.6 \times 0.026 \text{ mm}^3$ . Due to the small forces induced by the material, a custom-made stainless steel wire was characterized using two different methods and then used as a sensor to quantify bending forces using an optical microscope. It was shown that the chemical potential driving force for bending changes from linear to nonlinear as a function of the location of the water

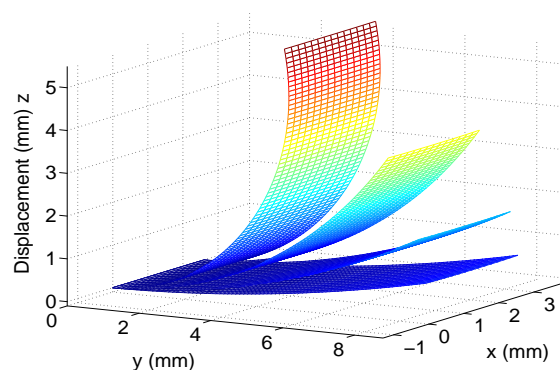


Fig. 10. The changes in free displacement bending was modeled by varying the chemical potential parameter  $h$  by factors of 2, 4, and 8. Bending monotonically increases as this parameter increases. The result is compared to the original case (smallest bending) previously plotted in Figure 8.

vapor source.

The experiments were correlated with a nonlinear continuum mechanics model that was coupled to a chemical potential energy function. It was necessary to include a higher order fourth order chemical free energy function to predict bending forces when the water vapor source approached the film surface. A linear chemical potential was sufficient to predict bending as this distance increased. These bending forces were predicted by writing the energy function in the spatial domain and correlating the free energy with energy in the reference configuration. Such coupling gives hydrostatic deformation from changes in water concentration without introducing explicit phenomenological coupling coefficients. By coupling this water concentration induced stresses with “mechanically” induced stresses from elasticity of the polymer network, bending deformation was predicted. Different amounts of bending deformation were predicted along the long and short axis of the film due to the orthotropic elastic properties. This required computing steady state concentration variations through the material thickness with the location of an external water vapor source.

The constitutive model and finite element model utilized concentration variations to determine hydrostatic stresses. Since these materials include liquid crystals which promote water absorption, additional underlying liquid crystal order-disorder processes and changes in charge density may occur as other chemicals in the air diffuse into the material. However in the present case, coupling with water vapor absorption was found to be sufficient to predict bending over a relatively wide range water vapor concentrations. In other cases, differences in pH and polarity of the solution can affect the amount of bending [7]. This would require chemical driving forces that are a function of the pH or the introduction of electrostatics and charge density variations. Moreover, liquid crystal networks that have an induced chirality

either from cholesteric liquid crystals or from rotation of a nematic phase through the film thickness would require more advanced modeling techniques that include liquid crystal director mechanics coupled to the polymer network.

It should also be noted that these films degraded after repeated exposure to a humid environment and after being stored in a desiccant container for several months. The concentration dependent bending results presented here were conducted over approximately an hour to ensure repeatable results. Several days and weeks later, the materials degraded in performance until no water vapor induced deformation occurred, although the materials were stored in a desiccant container. The nematic liquid crystal phase used in this composition may play a role in this irreversible behavior. Cholesteric compositions have also been tested where it has been suggested that improved reliability can be achieved [6]. The interactions between the liquid crystal phases, director order-disorder absorption process, and polymer network mechanics should be tested and modeled in further detail to understand this behavior.

It was also shown that the elastic modulus measurement was reduced by one to two orders of magnitude relative to dynamic mechanical analysis measurements [9]. Specimen or synthesis variability may be responsible for these variations in stiffness. However, these moduli measurements were conducted using bending mechanics which has been shown to predict lower moduli relative to uniaxial tension tests [10]. Despite this discrepancy, the mechanical bending experiments resulted in a relatively constant elastic modulus prediction based on classic beam theory as the point load approached the clamped edge of the film. This suggests reasonably ideal clamped boundary conditions which were further confirmed by comparing bending deformation near the clamp with classic beam theory; see the Appendix.

In conclusion, the model fits illustrate relatively strong sensitivity to water vapor exposure and reasonable correlation with bending force data. This provides a highly sensitive chemical sensor that is potentially ideal for MEMS microfluidics, chemical sensing, and biomedical applications. Since liquid crystals can be functionalized for sensitivity to a broad number of chemical constituents such as biological enzymes, this provides an exciting avenue for developing novel biomedical sensors; however, improved reliability must be achieved for these applications.

## Appendix Water Vapor Concentration

The water vapor concentration is determined using the ideal gas law and water vapor table values. The mass of the gas is given by

$$m_{gas} = MW_{gas} \frac{PV}{RT} \quad (18)$$

where  $MW_{gas}$  is the molecular weight of the gas,  $P$  is pressure,  $V$  is volume,  $R$  is the gas constant, and  $T$  is temperature.

The molecular weight of the gas is based on air and water vapor according to

$$MW_{gas} = y_{air}MW_{air} + y_{H_2O}MW_{H_2O} \quad (19)$$

where the molecular weight of air is  $MW_{air} = 29$  g air/mole air and  $MW_{H_2O} = 18.016$  g H<sub>2</sub>O/mole H<sub>2</sub>O. The mole fraction of each component is defined by  $y_i$ .

The mole fractions are determined based on saturated pressure and relative humidity. At room temperature and atmospheric pressure ( $T = 25^\circ$  C,  $P = 101.325$  Pa), the relative humidity is defined by  $h_r = P_{H_2O}/P_{H_2O}^*$  where  $P_{H_2O}^*$  is the saturated pressure. At room temperature and atmospheric pressure,  $P_{H_2O} = 2.8111$  Pa. The mole fractions can be computed based on the ratio of pressures,  $y_i = P_i/P$  therefore  $y_{H_2O} = 2.8111/101.325 = 2.774 \times 10^{-2}$  if  $h_r = 100\%$ . The mole fraction of air is thus  $y_{air} = 1 - y_{H_2O} = 0.97226$ .

Using (18) and (19), the mass of the gas is  $m_{gas} = 8.05 \times 10^{-11}$  kg gas. The number of moles of water is found from  $n_{H_2O}^{100\%} = y_{H_2O}n_{gas} = 7.785 \times 10^{-14}$  mol where  $n_{gas} = m_{gas}/MW_{gas}$ . Given the volume of gas above the liquid crystal LCN film,  $V_0 = 2.6 \times 8.8 \times 3$  mm<sup>3</sup>,  $c^{max} = n_{H_2O}^{100\%}/V_0 = 1.13 \times 10^{-6}$  mol/m<sup>3</sup>. The concentration scales with the relative humidity; therefore by applying  $h_r = 35\%$ , the concentration under ambient conditions is  $c_0 = 3.97 \times 10^{-7}$  mol/m<sup>3</sup>.

## Polynomial Fit

The parameters used in fitting the steady state diffusion relation in (13) are based on the following equations. For the linear fit the equation of a line is trivially satisfied by

$$\tilde{c}_w = 2.5 \times 10^{-4}(X - X_0)(1 - Y) + c_0 \quad (20)$$

where a normalized coordinate  $Y$  has been introduced. This coordinate is related to the material thickness coordinate by  $Y = \frac{1}{2}(\frac{Z}{t} + 1)$  where  $t$  is the LCN film thickness and the origin of  $Z$  is in the center of the film's thickness. For the non-linear steady state diffusion problem, the water vapor concentration is

$$\tilde{c}_w = 2.5 \times 10^{-4}(X - X_0)(a_1Y^9 + a_2Y^8 + a_3Y^7 + a_4Y^6 + \dots + a_5Y^5 + a_6Y^4 + a_7Y^3 + a_8Y^2 + a_9Y + a_{10}) + c_0 \quad (21)$$

## Film Modulus Analysis

The modulus measurement were based on optical microscopy comparisons of bending deformation versus classic beam theory. Images of the bending deformation were directly compared with beam displacement predictions using linear elastic theory of beams [8]. For a cantilever with a concentrated load  $P$  at a variable point along the length of the beam  $x$ , the displacement versus force relation is

Table 1. Polynomial coefficients used in (21).

Name	Value
$a_1$	$-1.27 \times 10^3$
$a_2$	$5.34 \times 10^3$
$a_3$	$9.37 \times 10^3$
$a_4$	$8.88 \times 10^3$
$a_5$	$-4.92 \times 10^3$
$a_6$	$1.61 \times 10^3$
$a_7$	$-2.98 \times 10^2$
$a_8$	2.81
$a_9$	-1.42
$a_{10}$	1.01

$$w(x) = \frac{Px^2}{6EI} (3a - x) \quad (22)$$

for the region between the clamped edge and the concentrated load ( $0 < x < a$ ). The modulus and moment of inertia are  $E$  and  $I$ , respectively. Plots of this solution in comparison with microscopy measurements are given in Figures 11 and 12. The images correspond to the modulus from Figure 4 for the normalized distances of 0.35 and 1. The comparisons of deformation illustrate good predictions using classic beam theory.

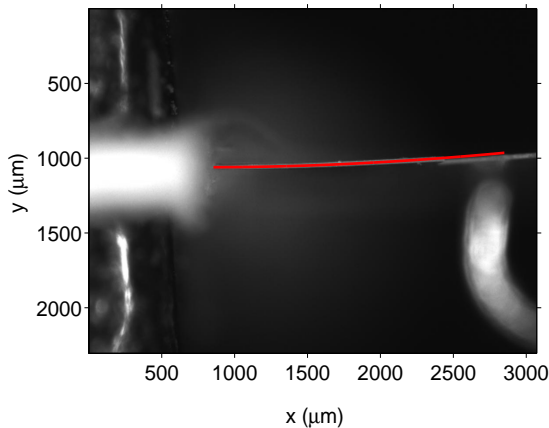


Fig. 11. Optical microscopy comparison of the film bending in comparison with classic beam theory. The film is clamped on the left and the wire point load is shown on the right for the case of the smallest normalized point load location of 0.35 from Figure 4.

#### Acknowledgments

This material is based upon work supported by the Florida Center for Advanced Aero Propulsion (FCAAP)

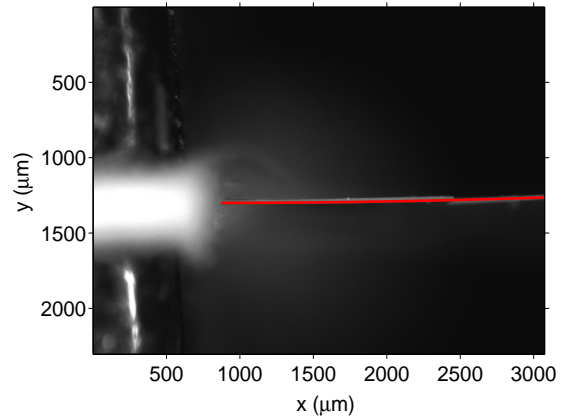


Fig. 12. Similar comparison of beam deformation microscopy measurement with classic beam theory as illustrated in Figure 11. The location of the point load was along the cantilever tip (i.e., normalized location of 1 in Figure 4).

and an AFOSR grant FA9550-09-1-0353. W. Oates and M. Hays also appreciate a Summer Faculty Fellowship Program through ASEE and Eglin AFRL. The authors also appreciate materials and synthesis help from Paul Luchette and Peter Palffy-Muhoray at the Liquid Crystal Institute at Kent State University.

#### References

- [1] Aßfalg, N., and Finkelmann, H., 2001. "A Smectic A liquid crystal elastomer (LSCE): Phase behavior and mechanical anisotropy". *Macromol. Chem. Phys.*, **202**, pp. 794–800.
- [2] Donnio, B., Wermter, H., and Finkelmann, H., 2000. "A simple and versatile synthetic route for the preparation of main-chain, liquid crystal elastomers". *Macromolecules*, **33**, pp. 7724–7729.
- [3] Warner, M., and Terentjev, E., 2007. *Liquid Crystal Elastomers—Revised Edition*. Oxford Science Publications, Oxford.
- [4] van Oosten, C., Harris, K., Bastiaansen, C., and Broer, D., 2007. "Glassy photomechanical liquid-crystal network actuators for microscale devices". *Eur. Phys. J. E*, **23**, pp. 329–336.
- [5] Urayama, K., Kohmon, E., Kojima, M., and Takigawa, T., 2009. "Polydomain-monomodomain transition of randomly disordered nematic elastomers with different cross-linking histories". *Macromolecules*, **42**, pp. 4084–4089.
- [6] Harris, K., Bastiaansen, C., Lub, J., and Broer, D., 2005. "Self-assembled polymer films for controlled agent-driven motion". *Nano Lett.*, **5**, pp. 1857–1860.
- [7] Harris, K., Bastiaansen, C., and Broer, D., 2006. "A glassy bending mode polymeric actuator which deforms in response to solvent polarity". *Macromol.*

- Rapid Commun.*, **27**, pp. 1323–1329.
- [8] Timoshenko, S., 1970. *Theory of Elasticity*. McGraw-Hill Companies.
- [9] Harris, K., Bastiaansen, C., and Broer, D., 2007. “Physical properties of anisotropically swelling hydrogen-bonded liquid crystal polymer actuators”. *J. Microelectromech. S.*, **16**(2), pp. 480–488.
- [10] Bayindir, Z., Sun, Y., Naughton, M., LaFratta, C., Baldacchini, T., Fourkas, J., Stewart, J., Saleh, B., and Teich, M., 2005. “Polymer microcantilevers fabricated via multiphoton absorption polymerization”. *Appl. Phys. Lett.*, **86**, p. 064105.
- [11] Bird, R., Stewart, W., and Lightfoot, E., 1960. *Transport Phenomena*. John Wiley and Sons, New York, NY.
- [12] P. de Gennes, and Prost, J., 1993. *The Physics of Liquid Crystals*. Oxford Science Publications, Oxford.
- [13] Oates, W., Wang, H., and Sierakowski, R., 2011. “A unified framework for modeling smart materials”. *in review*.
- [14] Moore, W., 1972. *Physical Chemistry*. Prentice-Hall, Inc., Englewood Cliffs, NJ.
- [15] Lupis, C., 1983. *Chemical Thermodynamics of Materials*. Prentice-Hall, New York.
- [16] Govindjee, S., and Simo, J., 1993. “Coupled stress-diffusion: Case II”. *J. Mech. Phys. Solids*, **41**(5), pp. 863–887.
- [17] Malvern, L., 1969. *Introduction to the Mechanics of a Continuous Medium*. Prentice-Hall, Inc., Englewood Cliffs, NJ.
- [18] Holzapfel, G., 2000. *Nonlinear Solid Mechanics*. John Wiley & Sons, Inc., Chichester.
- [19] Oates, W., and Wang, H., 2009. “A new approach to modeling liquid crystal elastomers using phase field methods”. *Modelling Simul. Mater. Sci. Eng.*, **17**, p. 064004 (21pp.).
- [20] Gurtin, M., 1996. “Generalized Ginzburg-Landau and Cahn-Hilliard equations based on a microforce balance”. *Physica D: Nonlinear Phenomena*, **92**(3-4), pp. 178–192.
- [21] Simo, J., and Fox, D., 1989. “On a stress resultant geometrically exact shell model. Part I: Formulation and optimal parameterization”. *Comput. Meth. Appl. Mech. Engrg.*, **72**, pp. 267–304.
- [22] Simo, J., Fox, D., and Rifai, M., 1989. “On a stress resultant geometrically exact shell model. Part II: The linear theory; Computational aspects”. *Comput. Meth. Appl. Mech. Engrg.*, **73**, pp. 53–92.
- [23] Taylor, R. L., 2010. *User manual of FEAP - - A Finite Element Analysis Program*. University of California at Berkeley.
- [24] J. Simo and D. Fox and M. Rifai, 1990. “On a stress resultant geometrically exact shell model. Part III: Computational aspects of the nonlinear theory”. *Comput. Meth. Appl. Mech. Engrg.*, **79**, pp. 21–70.
- [25] Simo, J., Rifai, M., and Fox, D., 1992. “On a stress resultant geometrically exact shell model. Part VI: Conserving algorithms for non-linear dynam-

ics”. *Int. J. Numer. Meth. Engrg.*, **34**, pp. 117–164.